Published version:

doi.org/10.1016/j.jaerosci.2012.01.001

Efficient Lagrangian simulation of electrospray droplets dynamics

Jordi Grifoll[a] and Joan Rosell-Llompart[a,b] *

[a]Departament d'Enginyeria Quimica, Universitat Rovira i Virgili, 43007 Tarragona, Catalunya, Spain

[b]ICREA (Catalan Institution of Research and Advanced Studies), Barcelona, Catalunya, Spain

e-mail addresses: jordi.grifoll@urv.cat , joan.rosell@urv.cat
* corresponding author. Tel. +34-977-558-660; fax: +34-977-559-621

Submitted to Journal of Aerosol Science

Keywords: electrospray, Lagrangian simulation, numerical simulation

Abstract

Tracking the trajectories of individual droplets in Lagrangian numerical simulations of electrosprays involves a large number of computations, due to the calculation of the electrostatic repulsion force between droplets (space charge force). Two strategies are proposed in this study to reduce such number while preserving accuracy. In one strategy, the force contribution from distant droplets is simplified by replacing the droplet charges belonging to small volumes or cells within the spray with a single charge per cell located at the cell's center-of-charge. In the other strategy, the integration of the droplets' motion in different axial regions of the spray is carried out using two very different time steps, using higher time resolution where the electrical force variation sensed by the droplets is larger. With these methods the CPU time was shortened by a factor of 39 (from 1658 to 42 hours), in a simulation of an electrospray characterized by a count mean diameter (CMD) of 8.84 micro-meter and around 26000 droplets in the steady state. In another spray, comprising about 3400 droplets (CMD=32 micro-meter), the CPU time was reduced by a factor of 4.4. In this case, the CPU reduction is smaller because the proposed methodologies become less efficient with a smaller number of droplets. This study is also concerned with the selection of a proper integration time step. We show that an acceptable upper bound to the time step is based on the proper description of numerical collisions between electrospray droplets. Interestingly, in both systems simulated, a similar maximum acceptable time step is found (2 micro-seconds).

1. Introduction

Electrospraying of liquids is a useful methodology to produce and control fine electrically-charged droplets. The methodology has been used in diverse applications including the production of thin and uniform coatings (Leeuwenburgh et al. 2006; Jaworek, 2007; De Jonge et al., 2009; Roncallo et al., 2010; Martin et al 2010), nanoparticle production (Barrero & Loscertales, 2007), space thrusters (Gamero-Castaño, 2008; Krpoun & Shea, 2009), and mass spectrometry (Fenn, 2003).

To electrospray a liquid in a gas environment, the liquid is emitted out of a capillary protrusion or tube set at a high voltage relative to a nearby electrode, such as a plate. Depending on the applied voltage, liquid flow rate, electrode configuration and the mechanical and electrical properties of the liquid, the electrospray can display different functioning modes (Cloupeau & Prunet-Foch, 1994). The so called *cone-jet mode* is usually the preferred mode as it produces uniform droplet sizes in a robust configuration. In this mode, a stable liquid meniscus, called Taylor cone, is formed at the tip of the capillary tube, and a jet is ejected from the cone apex. Upon break up, the jet leads to highly electrically charged droplets which travel through the gas phase driven by the electric field due to the electrodes and by the Coulombic repulsion between the droplets. Basic phenomena involved in the Taylor cone structure has been the subject of numerous studies (Fernández de la Mora & Loscertales, 1994; Gañan-Calvo, 2004; Higuera & Barrero, 2005; Fernández de la Mora, 2007; and others), whereas the dynamics of the formed droplets has received less attention, and is the focus of the present work.

The first detailed simulation of droplet dynamics in an electrospray was reported by Gañan-Calvo et al. (1994), who solved for each emitted droplet its momentum equation which included the electrical forces produced by the external field (due to the electrodes) and by the space charge (droplet-droplet Coulombic repulsion, including image charges at the plate), as well as the drag force due to friction between the droplets and the gas. The set of ODEs was solved using a modified Euler scheme for two test cases, each involving between 300 and 400 droplets. The numerical results were compared with experimental results to illustrate several electrosprays' spatial and statistical characteristics.

A similar approach was used by Hartman et al. (1999) to simulate the evolution of ethylene glycol droplets sprayed at various flow rates and nozzle-to-plate electrical

potentials. Only the droplet-droplet interactions for nearby droplets were considered in order to save computation time. After comparing their numerical simulation and experimental results they concluded for bimodal sprays that the droplet electrical charge scaled with the diameter raised to the 1.5 power, consistently with the experimental results of Tang and Gomez (1994). In addition, both Tang and Gomez (1994) and Hartman et al. (1999) concluded that the axial velocity of the surrounding gas at the spray axis can be significant (34% of the droplet axial velocity in the first study and 32% in the second). On the other hand, Gañán-Calvo et al. (1994) had made an order of magnitude analysis and concluded for their sprays that the characteristic gas velocity could be neglected compared to the droplet velocities. In general, however, the coupled motions of the two phases (gas and droplets) should be included in electrospray models.

Wilhelm et al. (2003) extended the Lagrangian model developed by Gañán-Calvo et al. (1994), adding droplet mass and heat transfer effects due to evaporation and the presence of a heated impinging plate. In their sprays, evaporation did not influence significantly droplet transport, but affected final droplet diameter and salt concentration. In a later study, Wilhelm and Madler (2006) applied the model to two distinct electrospray modes: the cone-jet and the intermittent multi-jet.

To understand and control film formation by electrospray, Rietveld et al. (2006) also used the model developed by Gañán-Calvo et al. (1994), except they did not consider the electrical forces between droplets under the assumption that they cancel out in the axial direction. This assumption conveniently reduced the computational effort, but is questionable in general.

Oh et al. (2008) analyzed the deposition characteristics from a twin nozzle electrospray configuration using the Lagrangian model. The ODE was integrated using the fourth-order Runge–Kutta method considering that the electrical forces were constant during an integration time step. In their different computational experiments there were between 3300 and 14500 droplets in the computational domain. This Lagrangian model was later applied to predict the deposition patterns obtained when a twin-nozzle electrospraying system is moved parallel to a collection plate (Jung et al., 2010).

Deng and Gomez (2007) noted the difficulties with Lagrangian models because, as a result of the droplet-droplet force calculations, the overall simulation time (CPU time) scales with N^2, where N is the number of droplets in the computational domain. To overcome this difficulty, they developed an alternative model in which the

computation of the droplet-droplet forces was simplified by modeling the spray space charge with a uniform line-of-charge on the spray axis. By this approach, they could capture the plume shape and other characteristics in a single electrospray. They later on applied this approximation to a system of multiplexed electrosprays with average primary droplet diameter around 11 micro-meters. It should be noted, however, that their system includes an extractor electrode between the Taylor cone and the spray plume, which provides a quasi constant droplet velocity. Also, for the multiplexed electrosprays the spray plume growth is limited by the presence of the other plumes. Both conditions (quasi constant drop velocity and small plume spread) help fulfill the assumptions of the uniform line-of-charge model. However, not all electrospray systems satisfy these conditions.

Recently, Yang et al. (2011) solved the Lagrangian-model droplet dynamics for the case of multiplexed electrosprays using a Personal Super Computer, based on Graphics Processing Units (GPUs), having a theoretical computational power of ~10 Tera FLOPS. The model allowed for tracking millions of droplet trajectories, and provided spray cloud structure and deposition patterns in good agreement with experimental results.

The aforementioned Lagrangian simulation studies have considered sprays with average droplet diameters equal or above 10 micro-meters, with the exception of Rietveld et al. (2006), who regarded much smaller diameters but ignored the droplet-droplet force calculations. On the other hand, most electrospray systems of technological interest generate droplets with average diameter in the micron or submicron range. The smaller droplet electrical mobilities of such systems result in denser sprays, with droplet numbers that can easily exceed $N \sim 10^4$. Without the use of a Super Computer, simulating such systems can take very long CPU times, eventually making simulations impractical as a predictive tool.

This *N*-square challenge is compounded by the need to identify a short enough time step for accurately tracking the droplets trajectories, especially near the emission point, where their velocities are high and the electrical force changes rapidly. Thus far, the time step is usually estimated using *ad-hoc* criteria (such as some fraction of the jet break up time), and is proven suitable by trial and error. This is a time consuming strategy for highly populated sprays, for which it would be useful to have a procedure to anticipate, at least, the order of magnitude of the integration time step.

In the present study, we have aimed to address both of these challenges. The first objective is thus to find a procedure to estimate an upper bound time step compatible with a realistic simulation of the electrospray droplets dynamics. The second and main objective is to propose and evaluate numerical strategies designed to speed up the simulations, by simplifying the droplet-droplet interaction calculations without compromising accuracy. In the first strategy, the number of droplet-to-distant droplet force computations is reduced by replacing the droplet point charges in the various distant regions of the spray by a much smaller number of lumped charges. The second strategy considers different time steps for different zones of the electrospray, in order to only track with high time resolution (with a small integration time step) the fastest droplets in the spray, while tracking the slower droplets much less frequently. The effectiveness of these two approaches has been quantified for two electrospray systems taken from the experimental literature.

2 Governing Equations and Numerical Procedures: Base Code

A base code for computing the droplet trajectories was developed before implementing numerical efficient strategies (described in Section 3). The base code is build upon a simple physical model of the simulated electrosprays, and accounts for all of the droplet-droplet electrostatic interactions responsible for the inefficiency in Lagrangian calculations of electrosprays. In this section, (i) we describe the model and the numerical procedures included in this base code, (ii) we introduce the *electric variation time* as a characteristic time to which the integration time step should scale, and (iii) we report on our code verification results.

2.1 Model

We integrate the equations of motion of electrospray droplets in the commonly encountered electrode configuration comprising a capillary tube (of semi-infinite length) that faces a planar collection plate (of infinite extent). The motion of a spray droplet i is described by its position vector $\mathbf{R_i}$ and velocity vector $\mathbf{V_i}$, which are functions of time (t), and are obtained by solving its equations of motion

$$\frac{d\,\mathbf{R_i}}{d\,t} = \mathbf{V_i} \quad ; \qquad \frac{d\,\mathbf{V_i}}{d\,t} = \mathbf{A_i} \tag{1a,b}$$

where $\mathbf{A_i}$ is the acceleration, i.e. the sum of forces acting on droplet *i* divided by its mass. The electrospray systems considered here comprise non-evaporating spherical droplets that interact with each other electrostatically, though not aerodynamically, and experience drag from the surrounding gas, which is assumed to be still air at normal conditions (1 atm, 20ºC). The droplet charge is assumed to remain constant in time and to stay uniformly distributed on the drop surface (i.e. resulting in a point-charge electric field). Under these constraints, Eq. (1b) becomes:

$$\frac{\pi}{6} d_i^3 \rho_d \frac{d\,\mathbf{V_i}}{d\,t} = -C_{Di} \frac{\pi}{8} d_i^2 \rho_g \mathbf{V_i} \left|\mathbf{V_i}\right| + q_i \mathbf{E_{ext}} + \frac{q_i}{4\pi\varepsilon} \sum_{i \neq j}^{N} q_j \left(\frac{\mathbf{R_{ij}}}{R_{ij}^3} - \frac{\mathbf{R_{iJ}}}{R_{iJ}^3} \right) - \frac{{q_i}^2}{4\pi\varepsilon} \frac{\mathbf{R_{iI}}}{R_{iI}^3} \tag{2}$$

where d_i is the droplet diameter (m), ρ_d is the liquid density (kg/m^3), ρ_g is the gas density (kg/m^3), C_{Di} is the drag coefficient, q_i is the droplet electrical charge (C), $\mathbf{E_{ext}}$ is the external electric field created by the potential difference between the electrodes (V/m), $\mathbf{R_{ij}} = \mathbf{R_i} - \mathbf{R_j}$ is the displacement between the position vectors of droplets *j* [$\mathbf{R_j} = (x_j, y_j, z_j)$] and *i* (m), and $\mathbf{R_{iJ}} = \mathbf{R_i} - \mathbf{R_J}$ is the displacement between the position vectors of the image of droplet *j* in the plate [$\mathbf{R_J} = (x_j, y_j, 2H - z_j)$] and droplet *i* (m) (where *H* is the separation between the capillary tip and the plate), ε is the air permittivity (taken as 8.854×10^{-12} A·s/V·m), and *N* is the total number of droplets in the plume. The drag coefficient in (2) has been calculated as

$$C_{Di} = \frac{24}{\mathrm{Re}_i} \left(1 + b\sqrt{\mathrm{Re}_i}\right)^2 \tag{3}$$

where $b = 0.1104$, and which is valid for $\mathrm{Re}_i = V_i d_i / \nu_g < 5000$ (ν_g is the gas kinematic viscosity) (Abraham 1970).

As stated in the introduction, the velocity of the surrounding gas can impact the droplet dynamics. Predicting the interactions between droplets and the gas phase would require solving the coupled equations governing droplet and gas phase dynamics.

Although this is out of the scope of this study, the numerical strategies herein developed for the droplet dynamics can be easily extended to include the gas phase velocity effects.

Solving Eqs. (1a,b) depends on having prior knowledge of different parameters and initial conditions. In addition to the aforementioned gas and liquid properties, these include $\mathbf{E}_{\mathbf{ext}}$, the droplet diameter and droplet charge joint distribution function, and the droplet coordinates and velocity vector at the emission point.

In this work, the external field, $\mathbf{E}_{\mathbf{ext}}$, was obtained from its electrical potential, ϕ, as

$$\mathbf{E}_{\mathbf{ext}} = -\nabla\phi \tag{4}$$

and the electrical potential was computed by solving Gauss' Law in terms of the Laplace equation

$$\nabla^2\phi = 0 \tag{5}$$

between the needle and the plate, for boundary conditions $\phi = \Phi_0$ at the needle and Taylor cone external surfaces, $\phi = 0$ V at the collection plate, $\partial\phi/\partial z = 0$ at $z = -10H$, and $\partial\phi/\partial r = 0$ at $r = 10H$. These two last boundary conditions were located sufficiently far from the spray, where they will not affect the external field values in the zone of forces calculation. Eq. (5) was discretized in cylindrical coordinates using the finite volume technique and was solved numerically on a very fine non-homogeneous grid. It should be noted that the influence of the droplet space charge on the needle surface charge distribution was neglected, whereas its effect on the collection plate was considered via image droplets as indicated in Eq. (2).

The droplets' diameters and electric charge should ideally be assigned in the code by randomly sampling the joint distribution function for droplet diameter and charge (constrained to additional rules of jet breakup, such as the alternation of primary and satellite droplets for Rayleigh breakup). Unfortunately, the joint distribution function has been investigated only for few electrosprays (de Juan and Fernández de la Mora, 1997; Gamero-Castaño, 2008). On the other hand, the diameter distribution is reported more often, and, furthermore, the mean droplet diameter has been shown to be predicted

by dimensional relationships (Fernandez de la Mora & Loscertales, 1994; Gañan-Calvo et al, 1997; Gañán-Calvo, 2004). Therefore, our code assumes a known droplet diameter distribution, from which droplets are created (i.e. randomly sampled). As droplets are created in a time step, they consume the liquid volume allocated for emission. As soon as a new droplet has a volume larger than the remaining volume budget, the creation of droplets stops. Such droplet is saved for emission at the start of the following time step. The volume allocated for emission is $Q \times \Delta t$ (where Q is the jet volumetric flow rate) plus the difference between the allocated and the actually emitted volumes of the previous time step; thus ensuring mass conservation. Note that rejecting this last droplet would result in a biased emission towards small droplets.

To every drop diameter created, an electric charge q_i is then assigned based on assumptions for the charge density (droplet charge per unit volume, $\rho_{qi} \equiv 6q_i / (\pi d_i^3)$). Based on an experimental investigation of the droplet diameter-charge joint distribution function, de Juan & Fernández de la Mora (1997) suggested that while for primary droplets q_i / d_i^3 is almost constant (indicating frozen charge during jet break-up in their sprays), the charge density of the satellite droplets and products of Coulomb explosions should be higher than for primary droplets. Gamero-Castaño (2008) confirmed these conclusions based on specific charge data for electrosprays in vacuum. Tang and Gomez (1994), one of the cases simulated in the present work, report the average charge densities and diameters for the primary and for the satellite droplets, which are scaled as $\bar{\rho}_{q,\mathrm{mode}} \sim \bar{d}_{\mathrm{mode}}^{-1.5}$, where "mode" refers to either "primary" or "satellite". In the other case simulated in the present work, Park et al. (2004), satellite droplets were not identified in the droplet size distribution, which was reported as a lognormal. In this case, we use the relationship ρ_{qi} = constant = I/Q (where I is the electrical current intensity).

Finally, to solve Eqs. (1a,b), the initial condition of each droplet is taken based on the velocity and position of the jet where it breaks up to form the droplets. The jet speed is not available usually, and must be estimated from the volumetric flow rate of liquid and the assumed or measured jet diameter. Here, the jet diameter was obtained from the count-mean droplet diameter $\bar{d}$ (or that for the primary droplets, in case of a bimodal distribution), according to the classical Rayleigh equation, $d_{jet} = \bar{d} / 1.89$, derived for uncharged jets (Chandrasekhar, 1981). It has been observed experimentally that this

relationship is very similar for charged as for uncharged jets (Jones & Thong, 1971; Tang & Gomez, 1994; Rosell-Llompart & Fernandez de la Mora, 1994).

Positioning the emitted droplets into the system requires further rules which are associated to the jet break up dynamics. Instead of such detailed information, we follow some logical rules, which, admitedly, suffer from some degree of arbitrariness. The initial axial coordinates of the droplets are distributed within an interval that starts at a distance l_0 from the end of the capillary tube. The length of this interval is equal to the jet speed times the time step duration. The transversal droplet emission coordinates (x_i, y_i) have been extracted from a Gaussian random distribution with zero average and standard deviation equal to two average droplet diameters. This small disturbance introduces the initial asymmetry that prevents emitting all the droplets into the same trajectory on the exact axis.

2.2 Integration scheme

Researchers in the field of Brownian Dynamics have developed several integration schemes for solving the Langevin equation, which faces the same main problem as Eqs. (1a,b), namely, that the electrical force calculations are the most computationally expensive part of the simulation. We have adopted the explicit integration of the drag force proposed by Ermak & Buckholz (1980).

Viscous drag forces and electrical forces in Eq. (2) can be implicitly written as

$$\frac{d\,\mathbf{V_i}}{d\,t} = -\frac{\mathbf{V_i}}{\tau_i} + \frac{\mathbf{F_i^{elec}}}{m_i} \tag{6}$$

where m_i is the mass of drop i and

$$\tau_i = \rho_d\, d_i^2 \Big/ \left[18\,\mu_g \left(1 + b\sqrt{\mathrm{Re}_i} \right)^2 \right] \tag{7}$$

is the drop viscous relaxation time, which tends to be independent of velocity as the Reynolds number decreases, μ_g is the dynamic viscosity of the surrounding gas ($\mathrm{N\cdot s/m^2}$).

Eq. (6) can be integrated twice at each time step from t to $t + \Delta t$, under the assumption that electrical forces ($\mathbf{F_i^{elec}}$) and τ_i remain constant in this time period, leading to

$$\mathbf{R_i}(t+\Delta t) = \mathbf{R_i}(t) + \left(1 - e^{-\Delta t/\tau_i}\right)\tau_i \mathbf{V_i}(t) + \frac{\mathbf{F_i^{elec}}(t)}{m_i}\tau_i^2\left(e^{-\Delta t/\tau_i} + \frac{\Delta t}{\tau_i} - 1\right) \quad (8)$$

To integrate Eq. (6) for the velocity at the end of the time step, the average between the electrical force values at the beginning and at the end of the time step is taken as the constant electrical force, to obtain

$$\mathbf{V_i}(t+\Delta t) = \mathbf{V_i}(t)e^{-\Delta t/\tau_i} + \frac{\mathbf{F_i^{elec}}(t+\Delta t) + \mathbf{F_i^{elec}}(t)}{2m_i}\tau_i\left(1 - e^{-\Delta t/\tau_i}\right) \quad (9)$$

Equations (8) and (9) are the basis of the Brownian Dynamics algorithm known as Ermak, which is recognized as being simple, efficient and accurate (Thalmann and Farago, 2007). Moreover, when the electrospray comprises small enough droplets for which Brownian movement is significant, Eqs. (8) and (9) should incorporate the stochastic terms that have been removed in this implementation (Ermak & Buckholz, 1980).

2.3 Time step selection

The ability of Eqs. (8,9) to accurately track a droplet trajectory depends on whether the time step Δt is small enough to ensure negligible changes of the electrical forces and of τ_i (which is not constant but, rather, dependent on $\mathbf{V_i}$ through Eq. (7)). In Eqs. (8) and (9) the value of τ_i at the beginning of the time step is taken as the representative constant value along the integration. To evaluate the error introduced by assuming its constancy, Eq. (6) has been integrated without the electrical forces term under two scenarios: (i) considering τ_i constant, and (ii) taking the two first terms of the Taylor expansion of $\mathbf{V_i}/\tau_i$ as dependent on $\mathbf{V_i}$ according Eq. (7). Upon comparing the two solutions we conclude that the error introduced by considering τ_i to be constant is

not significant as long as $\Delta t < \tau_i$ and Re_i is low or moderate. For example, when $\Delta t / \tau_i = 0.01$, the local error is 0.001% for $Re_i = 10$, rises to 0.003% when $Re_i = 100$, and is still as low as 0.3% when $\Delta t / \tau_i = 0.10$ and $Re_i = 100$.

Once the constancy of τ_i is assumed, the only limitation in the integration procedure for Eq. (2) is the assumption that the electrical force sensed by the droplet remains constant during the time step. We define the characteristic time for variation of the electrical force, here named *electric variation time*, $t_{ev,i}$, as the time that droplet i located at position (x_i, y_i, z_i) would need to sense a 100% difference on the electrical force that is acting upon it, under the conditions prevailing at (x_i, y_i, z_i), which is given as

$$t_{ev,i} = \left(\frac{1}{\left|\mathbf{F}_\mathbf{i}^{\mathbf{elec}}\right|} \left| \frac{d\mathbf{F}_\mathbf{i}^{\mathbf{elec}}}{dt} \right| \right)^{-1} \tag{10}$$

This $t_{ev,i}$ value is a function of time and position. Its order of magnitude can be estimated along the centerline, *a priori* of a simulation, by neglecting the effect of the space charge, as

$$t_{ev,CL}(z) = \left[\left| \frac{d \ln E_{ext,z,CL}}{dz} \right| v_{z,CL} \right]^{-1} \tag{11}$$

where $E_{ext,z,CL}$ is the axial component of the external electric field along the centerline, and $v_{z,CL}$ is the axial velocity of a single droplet of average diameter computed along the central axis, considering only its drag and external electric field forces. Its minimum value, $t_{ev,min}$, is located at the axial emission point, where the external field gradients are maximum while the droplets' velocity varies slowly:

$$t_{ev,\min} = \left[\left| \frac{d \ln E_{ext,z,CL}}{dz} \right|_{z=l_0} v_0 \right]^{-1} \tag{12}$$

where v_0 is the jet velocity. The time step Δt should be a fraction of $t_{ev,min}$ such as to ensure a nearly constant $\left|\mathbf{F}_i^{elec}\right|$ during the integration step.

2.4 Numerical code verification

Our base code based on the integration scheme described in section 2.2 has been verified using the parameters and system characteristics initially reported by Gañan-Calvo et al. (1994) and later on used by Wilhelm et al. (2003) to validate their code (Table 1). The external field of the system was calculated using the same approximation as used by these authors, instead of as outlined in section 2.1.

Eqs. (8) and (9) have been applied with a time step of $\Delta t = 10^{-6}$ s. We have tested that a $\Delta t = 2\text{x}10^{-6}$ s does not appreciably change the results. Fig. 1 shows the evolution of the liquid flow collected on the collection plate. To filter out the natural large fluctuations arising from the individual droplets impinging on the plate, the flow has been transformed using a Symmetrical Moving Average filter with a time width equal to the time taken by the first emitted droplets to travel from the emission point to the collection plate, in this case 2.5×10^{-3} s.

We consider that the system has achieved the steady state as soon as the averaged impinging flow exceeds the emitted flow, which occurs at $t_{ss} = 0.013$ s (Fig. 1). Beyond this time, the averaged number of droplets in the spray plume equals 498.2.

Wilhelm et al., (2003) pointed out that the simulation results are sensitive to the simulated jet break-up position. However, neither Gañan-Calvo et al. (1994) nor Wilhelm et al. (2003) reported the numerical value of the jet break-up position. We have found best agreement with Wilhelm et al.'s simulation for $l_0 = 0.38$ mm. Figs. 2a-f compare the results of Wilhelm et al (left side) with ours (right side) for: the spatial location of the droplets for a given snapshot (Fig. 2a,b), the plume average axial velocity as a function of the axial coordinate (Fig. 2c,d), and the axial velocity distribution at three axial positions (Fig. 2e,f). We conclude that our simulations agree reasonably well with the reported results by Wilhelm et al. (2003). It should be noted that the droplets acceleration towards the collection plate by image force attraction is unappreciable in both our simulations and Wilhelm et al.'s, in contrast to Gañan-Calvo et al.'s (Figs. 2c,d).

3. Numerically Efficient Approaches

As mentioned in the Introduction section, fully accounting for the droplet-droplet electrical interactions consumes most of the CPU time, because $N\times(N\text{-}1)/2$ droplet-to-droplet force calculations must be performed at each time step. The two numerical strategies that are proposed here to speed the computation (reduce the CPU time) are named Lumped Space Charge (LSC), and Zonal Time Steps (ZTS).

3.1 Lumped Space Charge approach (LSC)

Similar computational challenges to those faced here have previously been addressed in other fields. For the gravitational N-body problem, Appel (1985) and Barnes and Hut (1986) suggested numerical strategies aimed at grouping the effect of distant bodies. These authors represented the universe as a tree-like structure with hierarchic subdivisions, taking advantage of the tendency of the bodies to cluster in some regions while leaving other regions empty. With this methodology, the computation time increases as $N\times\log N$ instead of N^2. Similar approaches have been used in the field of Molecular Dynamics Simulation in the technique known as PPPM (particle-particle/particle mesh) proposed by Eastwood and Hockney (1974).

Based on these successes, we have developed the Lumped Space Charge (LSC) approach, in which the force due to distant droplets on a given droplet is accounted for by lumping the charges of distant droplets into a smaller number of representative charges. The spray plume is subdivided into cells, and to each cell a lumped point charge (*cell charge*) is assigned whose magnitude equals the sum of the droplet charges within the cell, and whose position is the center of charge $\mathbf{R}^{c\,ch}_{m,n,p}$ defined as

$$\mathbf{R}^{c\,ch}_{m,n,p}=\frac{\sum_{a\in m,n,p}\mathbf{R}_a q_a}{\sum_{a\in m,n,p} q_a} \tag{13}$$

Here indices (m, n, p) identify the cell in question, while index a identifies the droplets within the cell.

Our cell grid generation exploits the cylindrical symmetry of the electrodes and of the electrospray (statistically). First a number N_s of equal thickness slices are created along the z direction between the emission point, $z = l_0$, and the collection plate, $z = H$ (Fig. 3a). Next, each slice is cut into a number N_r of concentric rings up to the edge of the spray envelope (Fig. 3b); thus, $N_r = N_r(m)$, where $m = 1, \ldots, N_s$. Finally, each ring is cut along the angular direction into N_α equally spaced cells. Within this configuration, each droplet belongs to a cell (m, n, p) where $1 \le m \le N_s$, $1 \le n \le N_r(m)$, $1 \le p \le N_\alpha$.

The space charge force on a droplet i belonging to a cell (m, n, p) is computed in two steps: (i) droplet-by-droplet for droplets (and their images) belonging to the same cell or to *neighboring cells*, and (ii) droplet-by-cell for distant cells (as well as the image of the cell charge). The *neighboring cells* of cell (m, n, p) are those cells sharing with it a face, an edge, or a vertex. When the (m, n, p) cell touches the z-axis, this scheme wrongly considers as distant, droplets which are spatially quite near (typically for droplets in $(m, 1, p)$ and $(m, 2, p\text{-}2)$). To avoid this problem, the neighboring cells of $n = 1$ cells include all cells in the second ring ($n = 2$) within the same cell slice m, as well as in one slice above and one slice below (m+1 and m-1).

The total number of cells, $N_{tc} = N_\alpha \sum_{m=1}^{N_s} N_r(m)$ is chosen trying to maximize computer efficiency (i.e. reduce the number of space charge force calculations). Given the total number of droplets in the electrospray plume N and the number of cells neighboring each cell N_{nc} (assumed constant for the sake of simplicity), the total number of droplet-cell calculations is approximated as $N(N_{tc} - N_{nc} - 1) \approx N N_{tc}$, where it has further been assumed that $N_{tc} >> N_{nc}$. In addition, the total number of droplet-to-droplet calculations can be estimated as $N[((N_{nc}+1)/2)(N/N_{tc})]$, where a homogeneous droplet number per cell N/N_{tc} is assumed. Under these assumptions, the optimum number of cells which minimizes the total number of point-charge force calculations, namely $NN_{tc} + N[((N_{nc}+1)/2)(N/N_{tc})]$, equals

$$N_{tc} = \sqrt{\frac{(N_{nc}+1)}{2} N} \tag{14}$$

Using a representative value for the neighboring cell number of $N_{nc} \cong 26$, Eq. (14) suggests an optimum number of cells, N_{tc}, between 580 and 1160 when the total number of droplets, N, ranges from 25000 to 100000.

In this work we have found that $N_\alpha = 16$ and $N_s = 10$ are adequate. To obtain N_r, rings are formed in the following way. The slice containing the maximum radius of the spray plume is identified, and the thickness of most external ring is set equal to the slice height, while the remainder ring faces in this slice are set at radii satisfying $r_n^\gamma - r_{n-1}^\gamma = \text{constant}$. Here, the constant exponent γ controls the cell morphology (e.g., $\gamma = 2$ forms rings with equal base area, and $\gamma = 1$ equally spaced rings). Preliminary electrical force calculations for the test cases presented later, indicated that $\gamma = 1.1$ reduces the overall error in the electrical force calculations. Finally, this ring structure is transferred to the other slices (see Fig. 3a). In sum, the parameters defining the cell grid chosen in this study are: $N_\alpha = 16$, $N_s = 10$, $\gamma = 1.1$.

Finally, it should be noted that the overall cell arrangement is a dynamic structure that is rebuilt periodically, adapting to the plume geometry as it evolves in time. Consequently, preparing the cell lists and adapting the cell structure to the spray plume is CPU time consuming. In order to save time, the cell lists and the grid structure are not updated at each time step, but only after the fastest droplet in the system has travelled a fraction of the slices height in the axial direction. In preliminary calculations a fraction of 20% of the slice height did not significantly affect the space-charge force calculation. Therefore, to ensure accuracy, we have used a fraction of 10% in the simulations.

3.2 Zonal Time Steps approach (ZTS)

As discussed in section 2.3, the appropriate time step for the simulation is, evidently, dependent on the droplets velocities and the electric field variation with position. For the electrospray configuration studied here (one capillary tube and a collection plate), the droplets move fastest near the capillary end, where they experience a rapidly changing electric field. Further downstream, however, the droplets are moving much slower, and the field changes more slowly. This picture is supported by the numerical simulations of Gañan-Calvo et al. (1994) and Wilhelm et al. (2003), and by

the experimental results of Tang and Gomez (1994), in which the droplets' axial velocity reaches a maximum close to the emission point. Therefore, and according to the arguments of section 2.3, it is clear that the time step size used in our numerical scheme is restricted by the conditions prevailing close to the emission point, while, away from this region, much longer time steps could be used without compromising the accuracy of the integration.

In the Zonal Time Steps (ZTS) approach, the spray is divided into a Zone I located close to the emission point, where a small time step (Δt_I) is used, and a Zone II located downstream of Zone I, where a multiple of Δt_I is used as time step (Δt_{II}). In order to define these regions without actually carrying out the complete simulation using the Base Code, the droplet's velocity is first estimated by solving Eqs. (2) and (1a) for a droplet of average diameter injected at the axis center, without considering the space charge contribution to the electric field; namely, neglecting the third and fourth terms of the RHS of Eq. (2).

As implemented here, we take advantage of the LSC cell structure, and procedure for computing electrical forces between droplets. The boundary between Zones I and II is chosen as that between slices m_I and m_I+1, such that within m_I the estimated t_{ev} at the centerline has decreased two orders of magnitude from its maximum value. Then, the ZTS code proceeds in a loop. First, the droplets belonging Zone I are advanced ($\Delta t_{II}/\Delta t_I$ – 1) times with a time step Δt_I, with the electrical forces in Eqs. (8) and (9) calculated by the LSC procedure. Then, all the droplets in the system are advanced once by the LSC procedure, with a time step Δt_I if the droplet belongs to Zone I or Δt_{II} if the droplet belongs to Zone II.

4. Results and discussion

The model described in section 2 has been applied with and without the LSC and ZTS techniques described in section 3, in order to quantify the savings in computer resource they bring about. In order to simulate realistic situations, two test cases have been chosen from the experimental literature, for which droplet evaporation is negligible. Their geometrical and operating parameters, and liquid properties are provided in Table 1. Case I corresponds to an experiment reported by Park et al. (2004) in which ethanol was electrosprayed at 20 μL/min, and the droplet size distribution was determined by laser diffraction and had a count mean diameter of 8.84 μm. Case II

corresponds to the experiment reported by Tang and Gomez (1994), in which the structure of an electrospray of heptane at a flow rate of 167 μL/min was determined by Phase Doppler Anemometry. The bimodal distribution of droplet diameters comprised quasi monodisperse primary droplets averaging 32.4 μm in diameter. All simulations were run on a processor on a computation rack, an Intel(R) Xeon(TM) at 2.73 GHz.

4.1 Case I

(i) Complete simulation and time step selection using the Base Code

A key aspect of this computer simulation is the time needed to reach the steady state from a no-droplet condition at the beginning of the simulation. In the previous literature on computer simulation of electrosprays, the transient formation of the electrospray plume is not highlighted, probably because it took a small fraction of the total simulated time. On the other hand, Case I includes many more droplets (about 26000 in the steady state) and a large number of spray realizations must be sampled when interrogating the steady state for spray variables. After determining that the transient takes t_{ss} = 0.093 s (as determined by the procedure explained in section 2.4), we have chosen a total simulated time of 0.2 s.

In order to select the longest time step Δt that results in accurate droplets dynamics calculations for this system, we initially searched for an output variable that is sensitive to the time step by performing simulations with different time steps within the range $5\times10^{-7} < \Delta t < 2\times10^{-5}$ s. Output variables describing droplet distribution (such as radial flux distribution on the plate, droplets velocity distribution within the plume, and location of the plume envelope) turned out to have low sensitivity to Δt. On the other hand, snapshots of the droplets' position in the steady plume revealed droplets outside of the plume envelope, which increased in number as Δt increased. Such "outlier droplets" are clearly visible in the snapshots shown in Fig. 4 for time steps of 1×10^{-6}, 2×10^{-6} and 5×10^{-6} s. Analysis of the trajectories of these droplets prior to becoming outliers reveals that they were approached by other droplets to unrealistically short separations, and, as a result of the high repulsion forces, were accelerated wildly and thrown out of the spray plume. Notice that the Ermak integration scheme assumes that the forces remain constant and equal to their value at the beginning of the time step (see Eq.(8)).

Therefore, when a large time step is used, two droplets that collide at time $t + \Delta t$ may have barely noticed their mutual repulsion force at time t. In such collisions the conservation principles of momentum and energy are grossly violated, as they are numerical artifacts (not real).

The frequency of occurrence of such numerical collisions can be used for determining the largest time step consistent with accurate simulations. We have quantified these collisions at different time steps, by counting all droplet pairs characterized by a separation of their centers smaller than one count mean diameter at the end of each time step. These collision detection counts normalized per 1000 time steps are plotted in Fig. 5a as function of time step for $5\times10^{-7} \leq \Delta t \leq 2\times10^{-5}$ s. As initial condition in these simulations, we have used the droplets' positions and velocities at $t = 0.2$ s simulated using $\Delta t = 1\times10^{-6}$ s (as in Fig. 4a). They were then run for the period $0.20 < t < 0.25$ s using the different time steps. Fig. 5a shows that the collision detection rate decreases as the time step decreases, as expected, but levels out to a non-zero value for small Δt's, of approximately 11 counts/1000 steps. Such residual collisions are not numerical artifacts; rather, collision events taking place inside the numerical electrospray plume. Although the numerical results suggest the possibility of real collisions, these numerical events could also be consequence of the droplet injection rules and other simplifications within the model (Eqs (2)-(5)). As Δt decreases, the residual collisions eventually become sampled during several consecutive time steps, while the sampling frequency grows in inverse proportion to the decrease in Δt, thus leading to the constant Δt-independent asymptote shown in Fig. 5a. Because during residual collisions the interactions involve the most rapid changes in electric field experienced by any droplets in the spray, a suitable criterion for choosing an appropriate Δt can be based on proximity to the low-Δt asymptote of the collision count. By applying this criterion to Fig. 5a, we conclude that an appropriate Δt for this system should not exceed 2×10^{-6} s.

To further build upon this rationale, in Fig. 5b we have graphed the average number of time steps needed to describe each collision event for the same simulations as in Fig. 5a. When $\Delta t > 2\times10^{-6}$ s this number is almost one, indicating that Δt is not short enough to describe the details of each collision event (as they are detected only once). For $\Delta t \leq 2\times10^{-6}$ s, on the other hand, the average number of time steps increases above 1, becoming almost 4 for $\Delta t = 5\times10^{-7}$ s, as residual collisions are tracked. Therefore, $\Delta t = 2\times10^{-6}$ s has been chosen as the maximum acceptable time step.

In line with the arguments presented in section 2.3, we have checked that this maximum time step is a small fraction of the characteristic time for variation of the electric force, $t_{ev,min}$ (Eq. (11)). Indeed, for this system $t_{ev,min} = 1.05\times10^{-5}$ s.

In addition, the accuracy of the integration scheme depends on the near constancy of τ_i during the integration, as argued in section 2.2. For these simulations, on average $\tau_i = 1.3\times10^{-4}$ s, fulfilling also the requirement of $\tau_i >> \Delta t$.

The fraction of droplets involved in residual collisions in these simulations was 0.4 %, with 3200 residual collisions/s. When using $\Delta t = 10^{-5}$ s almost all collisions occurred close to the droplet emission point, with the farthest collision recorded at z = 6.1 mm and the maximum collision rate being located at z = 1 mm (the emission being at $z = l_0$ = 0.5 mm).

(ii) Simulations with LSC and ZTS strategies

The CPU times needed to perform the complete simulations of Figs. 4a-c with time steps of 1×10^{-6}, 2×10^{-6} and 5×10^{-6} s, were 1658, 835 and 341 hours for a system simulated time of 0.2 s (including the transient). These times are impractical for an acceptable accuracy (34.8 days at time steps of 2×10^{-6} s). With the lumped space charge field procedure (LSC) described in section 3.1, the 0.2 s system simulation using $\Delta t = 1\times10^{-6}$ s took a CPU time of 254 h, namely a reduction by a factor ~6.5 from the 1658 hours needed for the complete simulation. To assess the goodness of the LSC simulation, we have compared the mass fluxes impinging on the counterplate using the LSC technique and without using it (LSC Code versus Base Code). To avoid the spray transient, we took 500 snapshots uniformly distributed within the steady state period between 0.1 and 0.2 s to calculate the fluxes. Fig. 6 shows that the mass flux profile is almost identical in both cases, except possibly near r = 0, where the area used to compute the mass flux tends to zero as $r \rightarrow 0$ (symmetry axis), and, consequently, the uncertainty on the computed flux increases. In addition, the central region collected relatively few droplets. A total of 80698 droplets (80701 using the LSC technique) impinged on the plate in the period from 0.1 to 0.2 s, while only 45 (46 using the LSC technique) were collected in the area used to calculate the flux at r = 0. Because the mass flux is an average property, it does not inform about property fluctuations such as

droplet velocity, which, for instance, must be considered when predicting the structure of coatings. The two insets in Fig. 6 show that the probability density function of droplet axial velocities near the collector obtained by the three numerical methods are comparable.

The CPU time reduction achieved with the LSC Code is further improved with the Zonal Time Steps (ZTS) approach (section 3.2). Zone I has been located in the region $l_0 < z < 0.0064$ m, coinciding with the boundaries between second and third cell slices, and Zone II in $0.0064 < z < 0.03$ m (to the collection plate). The time step values chosen are $\Delta t_I = 1\times10^{-6}$ s for Zone I, and $\Delta t_{II} = 10\times\Delta t_I = 1\times10^{-5}$ s for Zone II.

Simulating the first 0.2 s of system time by the ZTS Code took 42 hours of CPU time, a factor of 39.5 times shorter than the complete simulation at $\Delta t = 1\times10^{-6}$ s. Fig. 6 shows that the mass flux distribution from this simulation is quite close to those for the LSC approximation and the complete simulation. The maximum discrepancy in mass flux with the complete simulation is 16% at $r = 0.001$ m. It appears that the fact of freezing the droplets in Zone II when using the small time steps, results in a tendency to keep the droplets closer to the z-axis. The mass flux distribution in Fig. 6 for the complete and ZTS simulations result in the same impinging mass flow rate, in which the higher ZTS flux near the axis is compensated by its lower flux near the plume edge.

4.2 Case II

(i) Complete simulation and time step selection using the Base Code

Tang and Gomez's 1994 experimental study, chosen as second case study (Table 1), helped quantify the mechanisms that govern the droplet formation and the spray structure, and provides measurements of the droplet distribution statistics for both primary and satellite droplets, while reporting radial and axial distributions of droplet diameter, number density and axial velocity, which can be useful for comparison with our numerical simulations. The diameter distributions for the primary and satellite droplets were taken as reported in Fig. 4a and 6a in Tang and Gomez's paper. In the code, the satellite droplets were created between primary droplets, with a ratio of number of satellites to primaries of 6:10.

To identify the appropriate time step for the numerical integration of the droplet motions, we ran the complete simulation in the range 5×10^{-7} s $< \Delta t < 5\times10^{-5}$ s, again for

a total system simulated time of 0.2 s. Fig. 7 shows the t = 0.2 s snapshots for Δt = 5×10^{-5} s and 5×10^{-7} s. Both simulations capture the plume structure reported by Tang & Gomez (1994), with a central plume formed by primary droplets and a shroud of satellite droplets. However, while the shroud's outer boundary is sharp for $\Delta t = 5\times10^{-7}$ s, the simulation using $\Delta t = 5\times10^{-5}$ s shows a diffuse boundary and the presence of many outlier droplets, both satellites and primaries. As noted earlier, the presence of outliers suggests an excessive time step, and the presence of artifact collisions. The variation of the collision rate and the average number of time steps taken by a collision event are presented in Figs. 8a,b. Fig. 8a shows that the collision rate for time steps under about $\Delta t = 2\times10^{-6}$ s becomes asymptotically constant, with a value around 1.3 collisions/1000 steps associated to residual collisions. In Fig. 8b, the average number of collisions describing each collision event increases rapidly from unity as the collision rate in Fig. 8a approaches its horizontal asymptote, below $\Delta t = 2\times10^{-6}$. Higher Δt values result in an average number of steps per collision event very close to 1, not enough to properly track the numerical collisions. In conclusion, it seems that the maximum time step for a proper simulation of the droplets dynamics in Case II is $\Delta t = 2\times10^{-6}$ s, which, interestingly enough, is the same value as was found for Case I. This maximum allowable time step is now only 1.2% of the characteristic time for variation of the electric field $t_{ev,min}$ (= 1.6×10^{-4} s). In conclusion, again in this case $t_{ev,min}$ is a suitable upper bound to the appropriate times step. This is because the electric field variations experienced by droplets during artifact collisions are much greater than merely as a result of variations of the external field.

In this system $\tau_i = 5.1\times10^{-4}$ s on average, while, because of the bimodal character of the droplet size distribution, the average value is $\tau_i = 1.3\times10^{-3}$ s for the primary droplets and $\tau_i = 1.4\times10^{-4}$ s for the satellites. In any case, these average values are well above the maximum time step $\Delta t = 2\times10^{-6}$ s, suggesting that the drag force calculation is well approximated.

To check the goodness of this simulation in describing the real system, Figs. 9a,b compare our radial distributions of droplet diameters and of number density against the experimental data by Tang & Gomez (1994). In both sets, the measured average droplet diameter remains almost constant till $r \sim 0.003$ mm, and decreases beyond this position. In the zone $0.0055 < r < 0.0065$ m, there is no agreement because no droplets were detected in the numerical simulations. Beyond r = 0.0065 m, the trend is recovered

although the experimental diameters are significantly smaller than those from the simulation. The reason for these disagreements is clarified by the radial distribution of the number density presented in Fig. 9b, which shows that the shroud of satellite droplets in the simulation is clearly shifted outward with respect to the real spray. Interestingly, the absolute value of the two relative maxima is very similar in both the experiment and the simulation. The central maximum, corresponding to the primary droplets, is experimentally located at r = 0.002 m, while the simulation has it at r = 0.0025m. The second peak was determined experimentally at around r = 0.007 m, while the simulation shows it at r = 0.0095 m. Thus, the simulation reproduces the main characteristics of the experimental system, although the plume shroud composed of satellite droplets is displaced radially outwards by about 2 or 3 mm with respect to the experimental data. One possible explanation for this effect is that our current numerical model does not take into account the effect of the axial wind created by the droplets, which was reported to be significant by Tang and Gomez (1994).

(ii) Simulations with the LSC and ZTS strategies

The CPU time required to run the complete simulation to system time t = 0.2 s with $\Delta t = 1\times10^{-6}$ s was 34.5 h. Use of the LSC methodology reduced this time by a factor of 1.25 only (having taken 27.7 h). The maximum reduction can be estimated considering the number of point-charge electrical force calculations given in section 3.1. The ratio of such calculations between the complete simulation and LSC is given as $(N-1)N_{tc}/\left[\left(N(N_{nc}+1)+2N_{tc}\right)\right]$. In this case, N = 3430 droplets and N_{tc} = 752 cells, which results in a maximum reduction of only 2.1. Therefore, the actual CPU time reduction is 60% of this maximum. Note that in Case I, the maximum reduction would similarly be estimated at 10.3, and that the actual reduction was also about 60% of this value.

As in Case I, the mass flux profile for the LSC simulation is very similar to the complete simulation profile, as shown in Fig. 10.

The system was also simulated with the ZTS procedure, using $\Delta t_I = 1\times10^{-6}$ s in region z < 0.0107 m and $\Delta t_{II} = 1\times10^{-5}$ s for z > 0.0107 m. With this procedure the total CPU simulation time was 7.8 h, a factor of 4.4 reduction relative to the complete simulation. Fig. 10 shows the radial profile of the mass deposition flux resulting from

this procedure, showing good agreement with the complete simulation, although with higher flux in the center of the plume, as noted earlier also in Case I. As for Case I, all three methods lead to similar droplet axial velocity fluctuations near the collector, as can be seen in the insets of Fig. 10.

Table 2 summarizes the CPU times obtained with the various code configurations for both cases studied. The differences in numerical efficiency between the two study cases support the expectation that as the number of droplets in the plume increases (finer droplets), the proposed LSC and ZTS procedures become more effective.

5. Conclusions

In Lagrangian simulations of electrosprays droplets dynamics, most of the computation CPU time is spent determining the electrical repulsion forces between droplets (space charge force). Such simulations can take an impractical long time when the spray comprises a large number of droplets N, for example, greater than several thousands. This is especially relevant when independent system realizations are needed for statistical averaging under steady state. In one case simulated in this study, where N exceeded 2.5×10^4 in the steady state, simulations took almost 10 weeks to simulate 0.2 seconds of system time.

We have assessed the efficiency of two numerical strategies designed to reduce the CPU time, while preserving accuracy. Both strategies are aimed at reducing the number of computations of the space charge force. Our first numerical strategy, called Lumped Space Charge (LSC) approach, is based on lumping droplets together in various cell volumes in the spray, and in computing only once the force from all droplets within each cell onto each distant droplet from the cell. The LSC approximation reduced the CPU time by a factor of 6.5 when simulating Case I, which is characterized by ~26000 droplet spray count in the steady state, and by a lognormal distribution of droplet diameters with count mean of 8.84 μm. This factor was improved to 39.5 by an evolution of the LSC approximation called the Zonal Time Step (ZTS) approach, which uses different integration time steps in different regions of the spray (shorter ones near the emission point).

For Case II, an electrospray comprising a bimodal droplet distribution, with 32.4 μm count mean primary droplet diameter, and 3430 droplets in the steady state, the CPU time was reduced by a factor of 1.25 with LSC, and of 4.4 with ZTS. These factors are lower with respect to Case I because the LSC and ZTS approximations become computationally more efficient as the number of droplets increases.

In both Cases I and II, the mass fluxes arriving at the collection plate have small differences between the approximate and the complete Lagrangian simulations, indicating very little loss of accuracy when using LSC.

Numerical collisions between droplets were identified in both of these sprays (Cases I and II). Because droplets undergoing collisions experience the largest variations in electric field, the capture of an average collision in consecutive time steps has been used as a criterion to select the integration time step. The largest acceptable time step describing such events was around 2 μs in both spray systems studied.

Acknowledgements

This work was financially supported with grant CTQ2008-05758/PPQ from the Spanish Ministry of Science and Innovation, and grant 2009-SGR-1529 from the Government of Catalonia, Spain.

References

Abraham, F. F. (1970). Functional dependence of drag coefficient of a sphere on Reynolds number. *Physics of Fluids, 13,* 2194-2195.

Appel, A. W. (1985). An Efficient Program for Many-Body Simulation. *Siam Journal on Scientific and Statistical Computing, 6,* 85-103.

Barnes, J., & Hut, P. (1986). A hierarchical O(N log N) force-calculation algorithm. *Nature, 324*, 446-449.

Barrero, A., & Loscertales I. G. (2007). Micro- and nanoparticles via capillary flows. *Annual Review of Fluid Mechanics, 39,* 89-106.

Chandrasekhar (1981). *Hydrodynamic and Hydromagnetic Stability*. Dover: New York.

Cloupeau, M., & Prunet-Foch, B. (1994). Electrohydrodynamic spraying functioning modes: a critical review. *Journal of Aerosol Science, 25,* 1021-1036.

De Jonge, L. T., Leeuwenburgh, S. C. G., Van Den Beucken, J. J. J. P., Wolke, J. G. C., & Jansen, J. A. (2009). Electrosprayed enzyme coatings as bioinspired alternatives to bioceramic coatings for orthopedic and oral implants. *Advanced Functional Materials, 19,* 755-762.

De Juan, L., & Fernandez de la Mora, J. (1997). Charge and size distributions of electrospray drops. *Journal of Colloid and Interface Science, 186,* 280-293.

Deng, W., & Gomez, A. (2007). Influence of space charge on the scale-up of multiplexed electrosprays. *Journal of Aerosol Science, 38,* 1062-1078.

Eastwood, J. W., & Hockney, R. W. (1974). Shaping the force law in two-dimensional particle-mesh models. *Journal of Computational Physics, 16,* 342-359.

Ermak, D. L., & Buckholz, H. (1980). Numerical-integration of the Langevin equation - Monte-Carlo simulation. *Journal of Computational Physics, 35,* 169-182.

Fenn, J. B. (2003). Electrospray wings for molecular elephants (Nobel lecture). *Angewandte Chemie-International Edition, 42,* 3871-3894.

Fernandez de la Mora, J. (2007). The fluid dynamics of Taylor cones. *Annual Review of Fluid Mechanics, 39,* 217-243.

Fernandez de la Mora, J., & Loscertales I. G. (1994). The current emitted by highly conducting Taylor cones. *Journal of Fluid Mechanics, 260,* 155-184.

Gamero-Castaño, M. (2008). The structure of electrospray beams in vacuum. *Journal of Fluid Mechanics,* 604, 339-368.

Gañan-Calvo, A. M., Lasheras, J. C., Davila, J., & Barrero, A. (1994). The electrostatic spray emitted from an electrified conical meniscus. *Journal of Aerosol Science, 25,* 1121-1142.

Ganan-Calvo, A. M., Davila, J., & Barrero, A. (1997). Current and droplet size in the electrospraying of liquids. Scaling laws. *Journal of Aerosol Science, 28,* 249-275.

Gañan-Calvo, A. M. (2004). On the general scaling theory for electrospraying. *Journal of Fluid Mechanics, 507,* 203–212.

Hartman, R. P. A., Borra, J.-P., Brunner, D. J., Marijnissen, J. C. M., & Scarlett, B. (1999). The evolution of electrohydrodynamic sprays produced in the cone-jet mode, a physical model. *Journal of Electrostatics, 47,* 143-170.

Higuera, F. J., & Barrero, A. (2005). Electrosprays of very polar liquids at low flow rates. *Physics of Fluids, 17,* 018104.

Jaworek, A. (2007). Electrospray droplet sources for thin film deposition. *Journal of Materials Science, 42,* 266-297.

Jones, A. R., & Thong, K. C. (1971). The production of charged monodisperse fuel droplets by electrical dispersion. *Journal of Physics D-Applied Physics, 4,* 1159-1166.

Jung, J. H., Oh, H., & Kim, S. S. (2010). Numerical simulation of the deposition pattern in multiple electrohydrodynamic spraying. *Powder Technology 198,* 439-444.

Krpoun, R., & Shea, H. R. (2009). Integrated out-of-plane nanoelectrospray thruster arrays for spacecraft propulsion. *Journal of Micromechanics and Microengineering, 19,* 045019.

Leeuwenburgh, S. C. G., Heine, M. C., Wolke, J. G. C., Pratsinis, S.E., Schoonman, J., & Jansen, J.A. (2006). Morphology of calcium phosphate coatings for biomedical applications deposited using Electrostatic Spray Deposition. *Thin Solid Films 503,* 69–78.

Martin, S., Garcia-Ybarra, P.L., & Castillo, J.L. (2010). Electrospray deposition of catalyst layers with ultra-low Pt loadings for PEM fuel cells cathodes. *Journal of Power Sources, 195,* 2443-2449.

Oh, H., Kim, K., & Kim, S. (2008). Characterization of deposition patterns produced by twin-nozzle electrospray. *Journal of Aerosol Science, 39,* 801-813.

Park, H., Kim, K., & Kim, S. (2004). Effects of a guard plate on the characteristics of an electrospray in the cone-jet mode. *Journal of Aerosol Science, 35,* 1295-1312.

Rietveld, I. B., Kobayashi, K., Yamada H., & Matsushige, K. (2006). Electrospray deposition, model, and experiment: Toward general control of film morphology. *Journal of Physical Chemistry B, 110,* 23351-23364.

Roncallo, S., Painter, J. D., Ritchie, S. A., Cousins, M. A., Finnis, M. V., & Rogers K. D. (2010). Evaluation of different deposition conditions on thin films deposited by electrostatic spray deposition using a uniformity test. *Thin Solid Films, 518,* 4821-4827.

Rosell-Llompart, J., & J. Fernandez de la Mora (1994). Generation of monodisperse droplets 0.3 to 4 [mu]m in diameter from electrified cone-jets of highly conducting and viscous liquids. *Journal of Aerosol Science, 25,* 1093-1119.

Tang, K., & Gomez, A. (1994). On the structure of an electrostatic spray of monodisperse droplets. *Physics of Fluids, 6,* 2317-2332.

Thalmann, F. & Farago, J. (2007). Trotter derivation of algorithms for Brownian and dissipative particle dynamics. *The Journal of Chemical Physics, 127,* 124109.

Wilhelm, O., Madler, L., & Pratsinis, S. E. (2003). Electrospray evaporation and deposition. *Journal of Aerosol Science, 34,* 815-836.

Wilhelm, O., & Madler, L. (2006). Cone-jet and multijet electrosprays: Transport and evaporation. *Atomization and Sprays, 16,* 83-102.

Yang, W., Lojewski, B., Wei. & Deng, W. (2011). Interaccions and deposition patterns of multiplexed electrosprays. *Journal of Aerosol Science,* doi:10.1016/j.jaerosci.2011.11.004.

Table 1. Liquid and electrospray system properties.

	Verification system	Case I	Case II
Liquid density (kg/m^3), ρ	685	789.4	685
Liquid flow rate (m^3/s), Q	2.4×10^{-9}	0.333×10^{-9}	2.78×10^{-9}
Outer needle diameter (m)	1×10^{-3}	9×10^{-4}	4.5×10^{-4}
Needle to plate distance (m), H	0.03	0.03	0.03
Needle to plate potential (V), Φ_0	5200	4000	5000
Electric current intensity (A), I	45×10^{-9}	37.4×10^{-9}	n.g.[¥]
Primary droplet diameter, count mean (m), $\bar{d}$	38×10^{-6}	8.84×10^{-6}	3.24×10^{-5}
Primary drop diameter, RMS (%)	4	20.9	2.02
Satellite droplet diameter, count mean (m)	n.a.[§]	n.a.[§]	9.93×10^{-6}
Satellite drop diameter, RMS (%)	n.a.[§]	n.a.[§]	25%
Jet break up position (mm), l_0	0.38	0.5[#]	2.4[£]
References	Gañan-Calvo et al., (1994); Wilhelm et al., (2003)	Park et al., (2004)	Tang and Gomez, (1994)

[§]n.a.: not applicable.
[¥]n.g.: not given.
[#]This value is chosen *ad hoc* at $13.5\times\bar{d}$ plus the Taylor cone height (0.39 mm).
[£]Taken from Fig. 7 of Tang and Gomez (1994).

Table 2. CPU time needed to perform the electrospray dynamics simulation from an initial condition of zero spray droplets until t = 0.2 s, using different methodologies and time steps.

Case	Methodology	Δt (s)	CPU time (h)
I	complete simulation	1×10^{-6}	1658
		2×10^{-6}	835
		5×10^{-6}	341
	LSC	1×10^{-6}	254
	ZTS	1×10^{-6} *	42
II	complete simulation	5×10^{-7}	69
		1×10^{-6}	34.5
		2×10^{-6}	17
		5×10^{-6}	7
		1×10^{-5}	3.5
		2×10^{-5}	2
		5×10^{-5}	1
	LSC	1×10^{-6}	27.7
	ZTS	1×10^{-6} *	7.8

*In ZTS the listed value is Δt_I; while $\Delta t_{II} = \Delta t_I \times 10$.

FIGURES

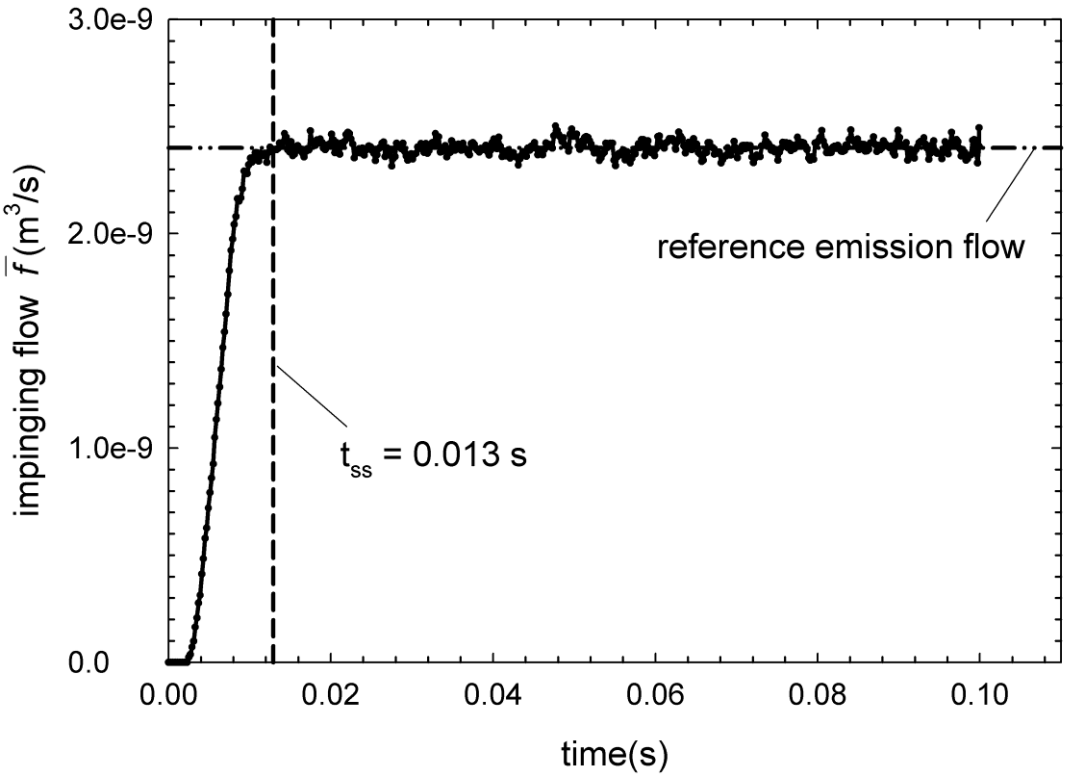

Fig. 1. Evolution of the impinging flow for the simulation of the code verification case.

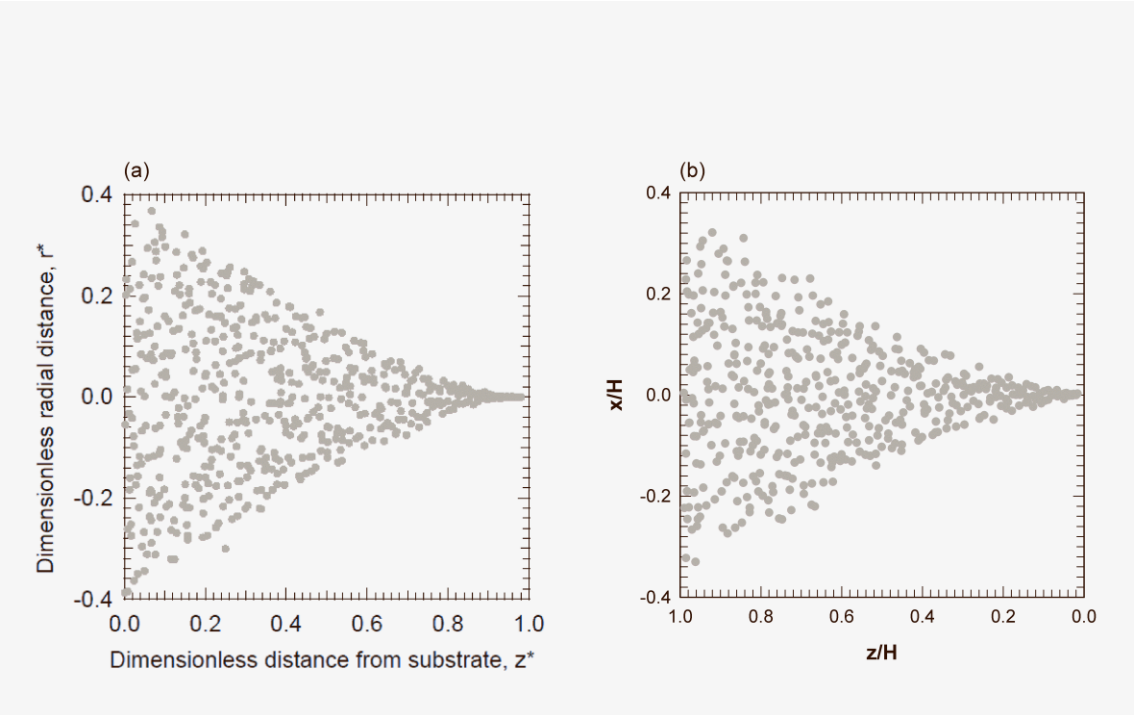

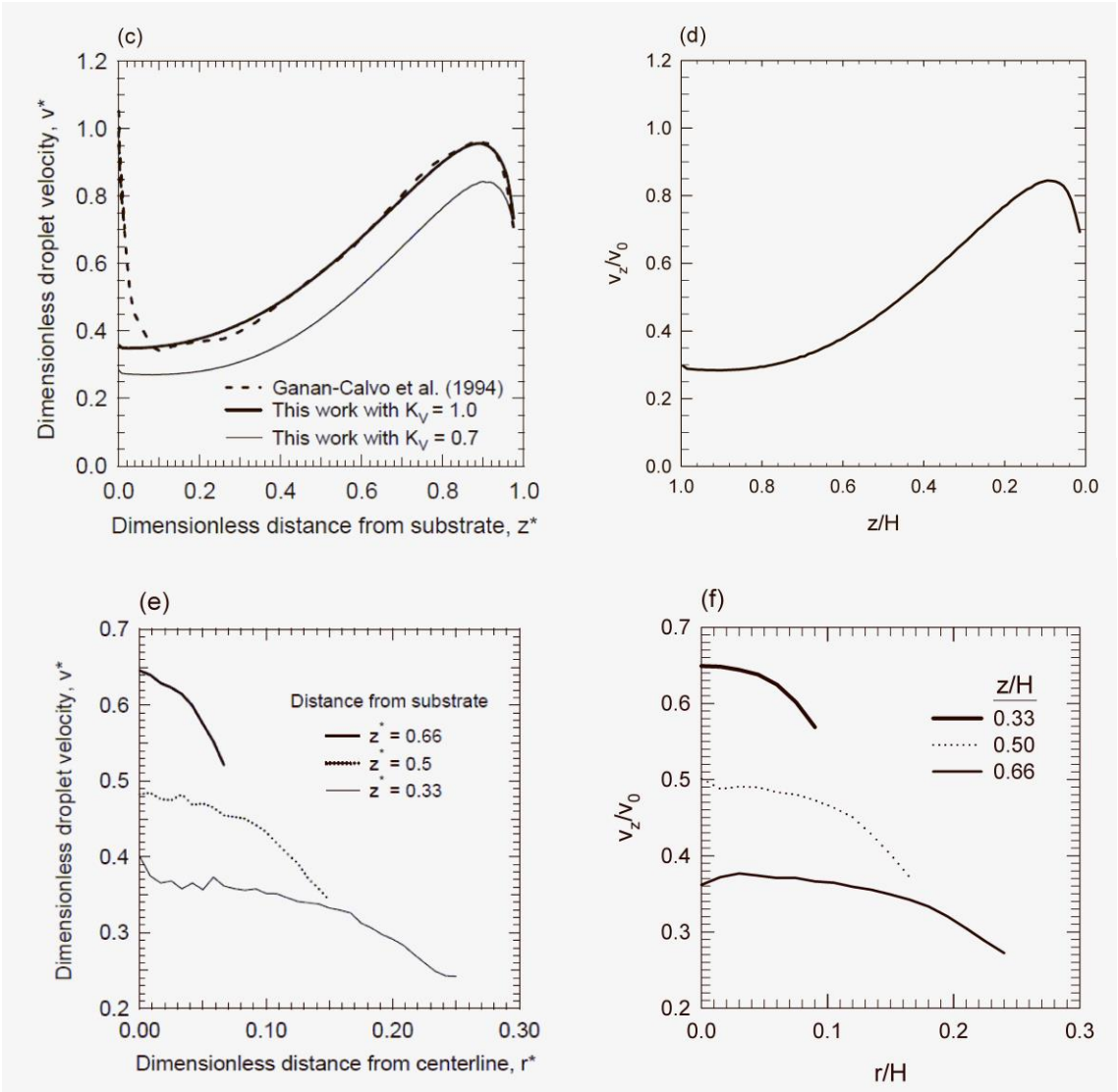

Fig. 2. Comparison between the code verification results reported by Wilhem et al. (2003) [a, c, e] and the present simulations [b, d, f]. Snapshot of the droplets spatial distribution (a, b). Transverse average axial velocity variation along the axis (c, d). Radial distribution of the axial velocity at different axial positions (e, f).

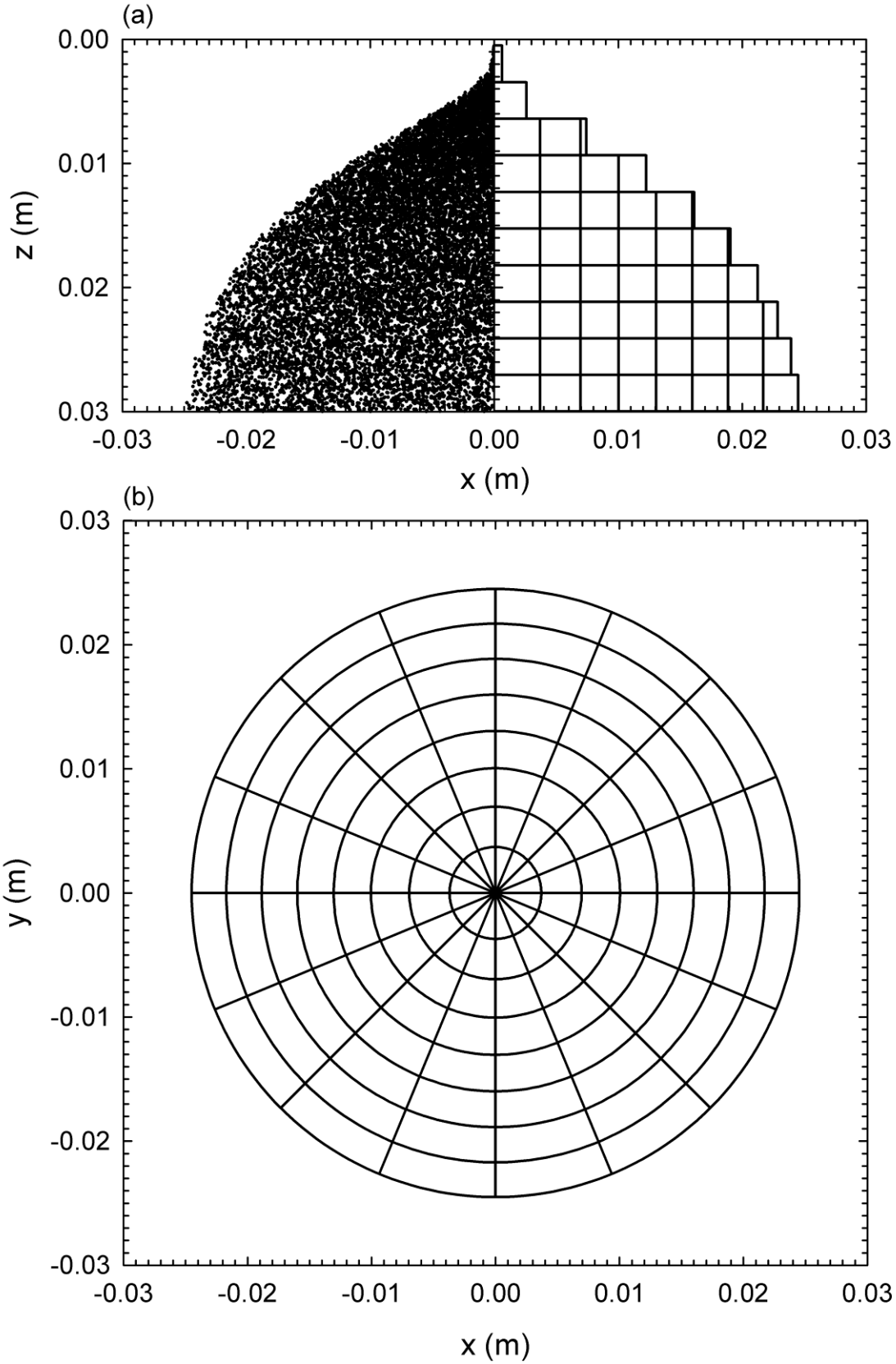

Fig. 3. Example cell grid configuration used in the LSC methodology. (a) Lateral view of an actual droplets snapshot (left) and its slices and ring divisions (right). (b) Sectional view showing ring and angular divisions for the slice closest to the collecting plate.

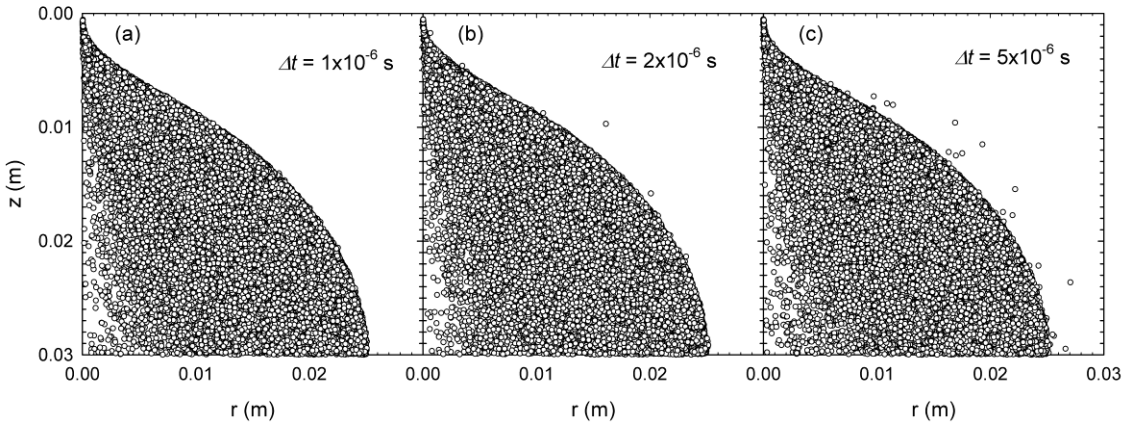

Fig. 4. Snapshots of the droplets positions at t = 0.2 s for Case I simulations using different Δt.

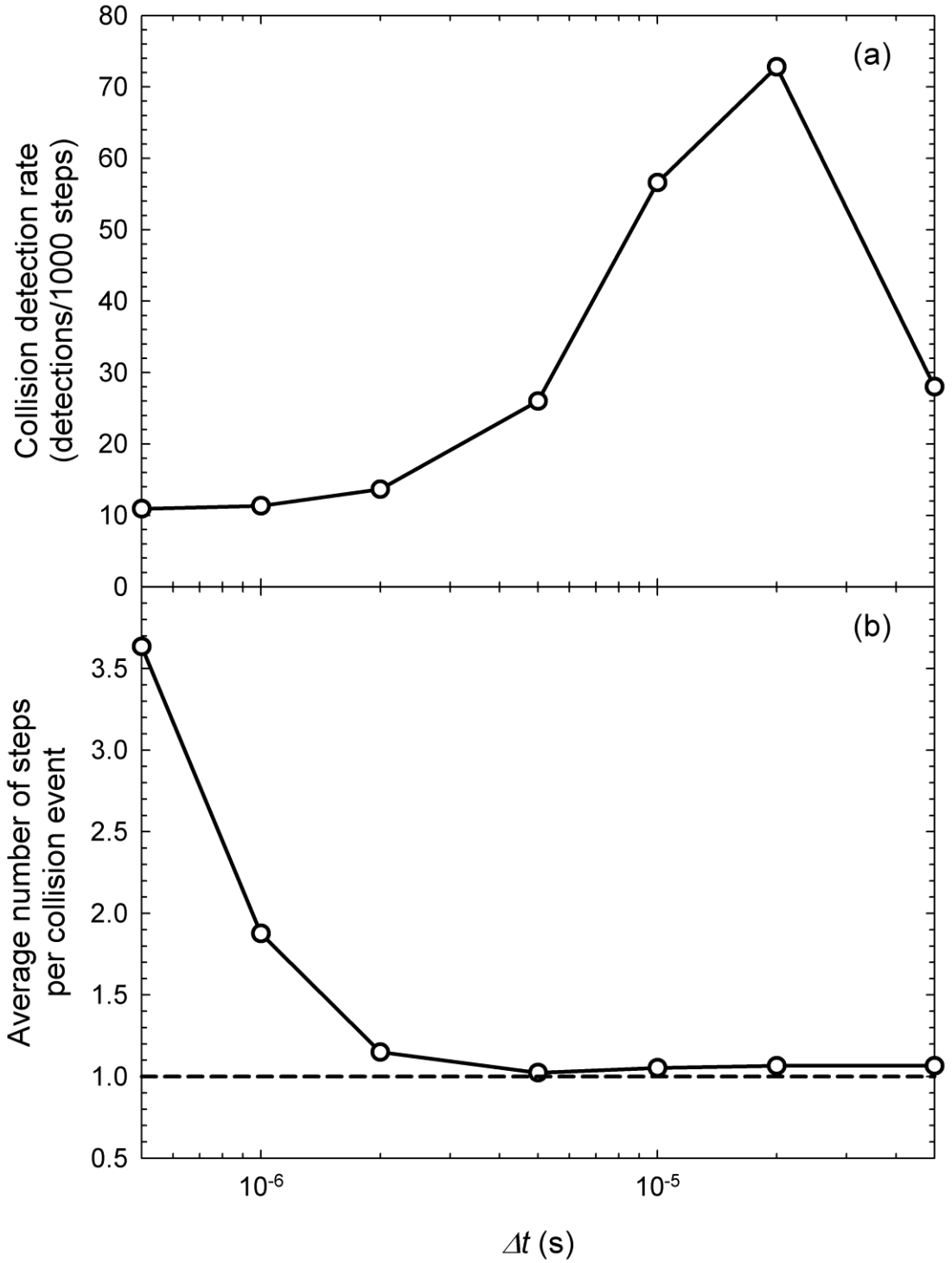

Fig. 5. Analysis of droplet collisions (as defined in text) for the steady state conditions of Case I. Simulations for $0.2 < t < 0.25$ s. (a) Collision detections each thousand steps for different Δt's. (b) Average number of consecutive time steps Δt in which collision events are found for different Δt's.

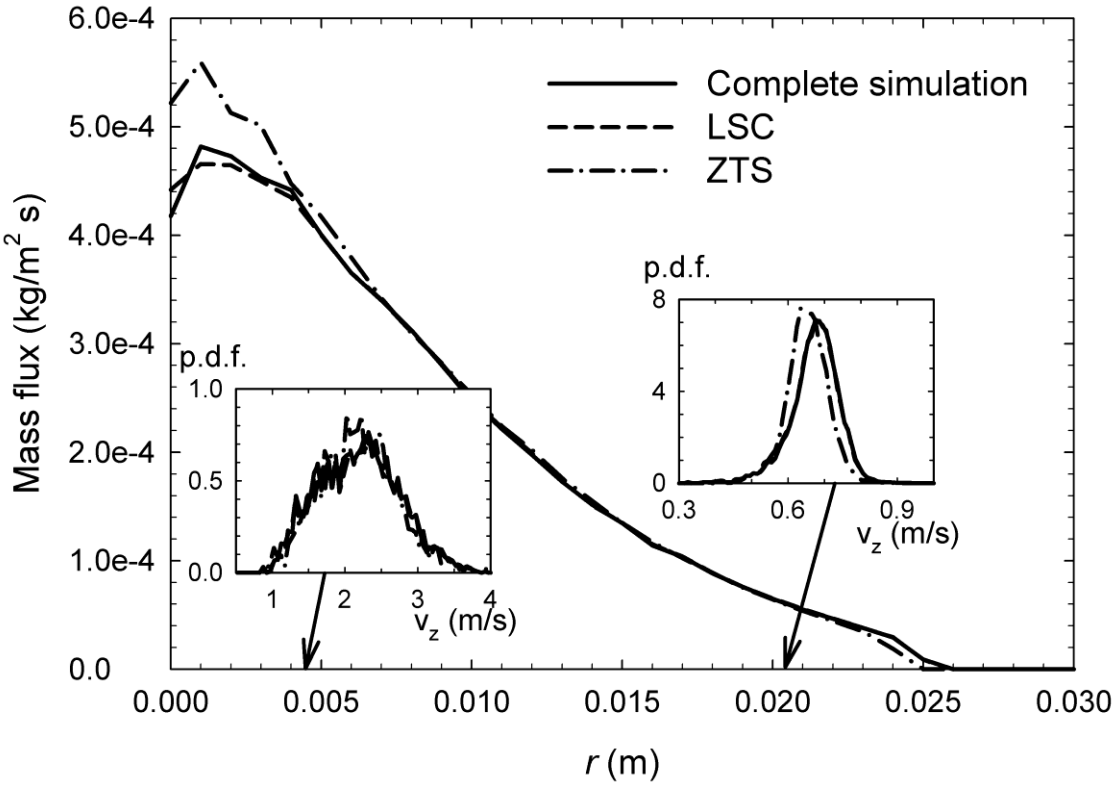

Fig. 6. Radial distribution of the mass flux due to droplets impinging on the collection plate, using different simulation methods for Case I. Insets show the p.d.f. (s/m) of axial droplet velocity located within 0.028< z < 0.029 m, and 0.004 < r < 0.005 m (left) and 0.020 < r < 0.021 m (right).

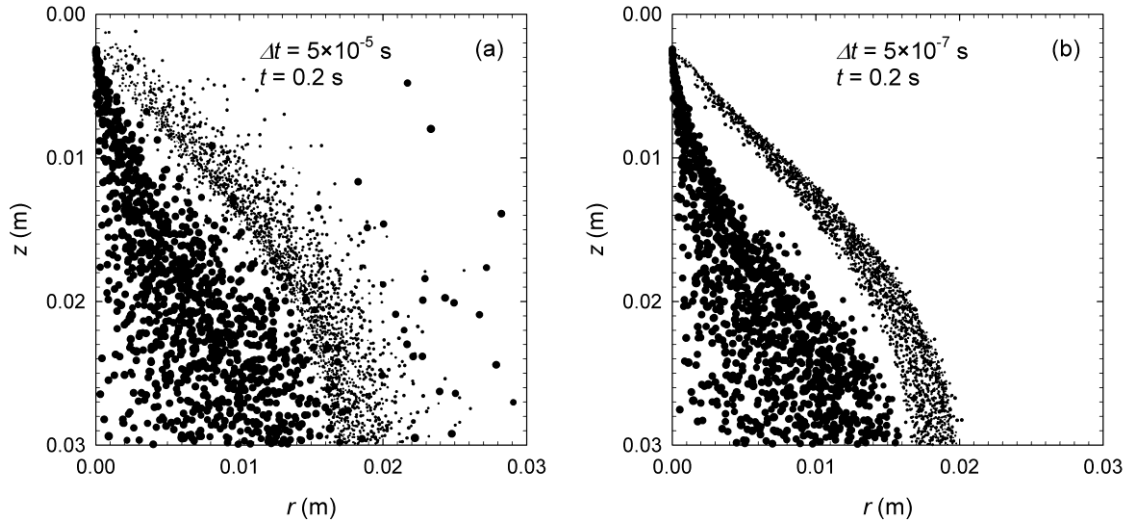

Fig. 7. Snapshots of the droplets positions at t = 0.2 s for Case II simulations for Δt = 5×10^{-5} and Δt = 5×10^{-7} s. Dot diameter is proportional to actual droplet diameter.

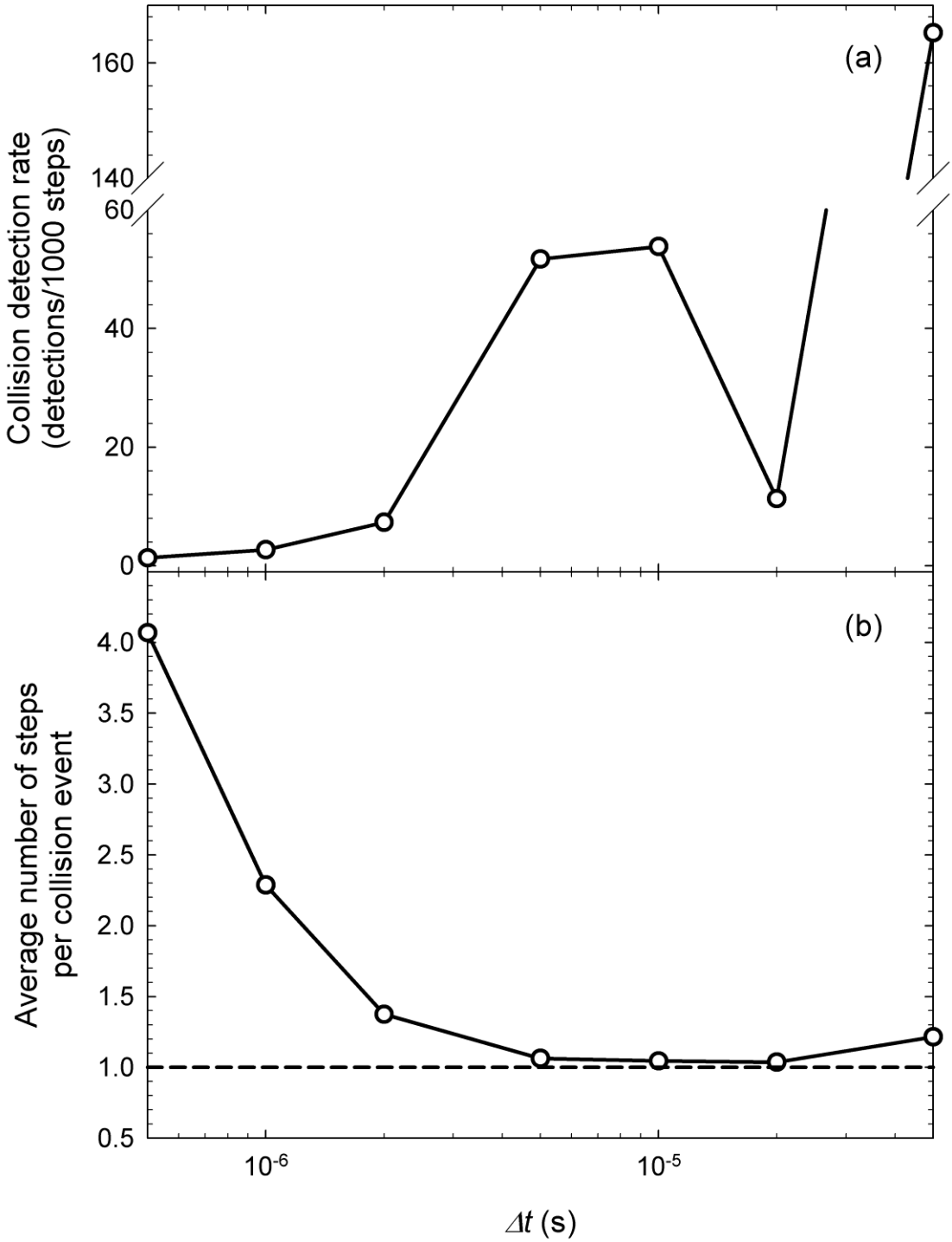

Fig. 8. Analysis of droplet collisions (as defined in text) for the steady state conditions of Case II. Simulations for $0.0 < t < 0.20$ s. (a) Collision detections each thousand steps for different Δt. (b) Average number of consecutive time steps Δt in which collision events are found.

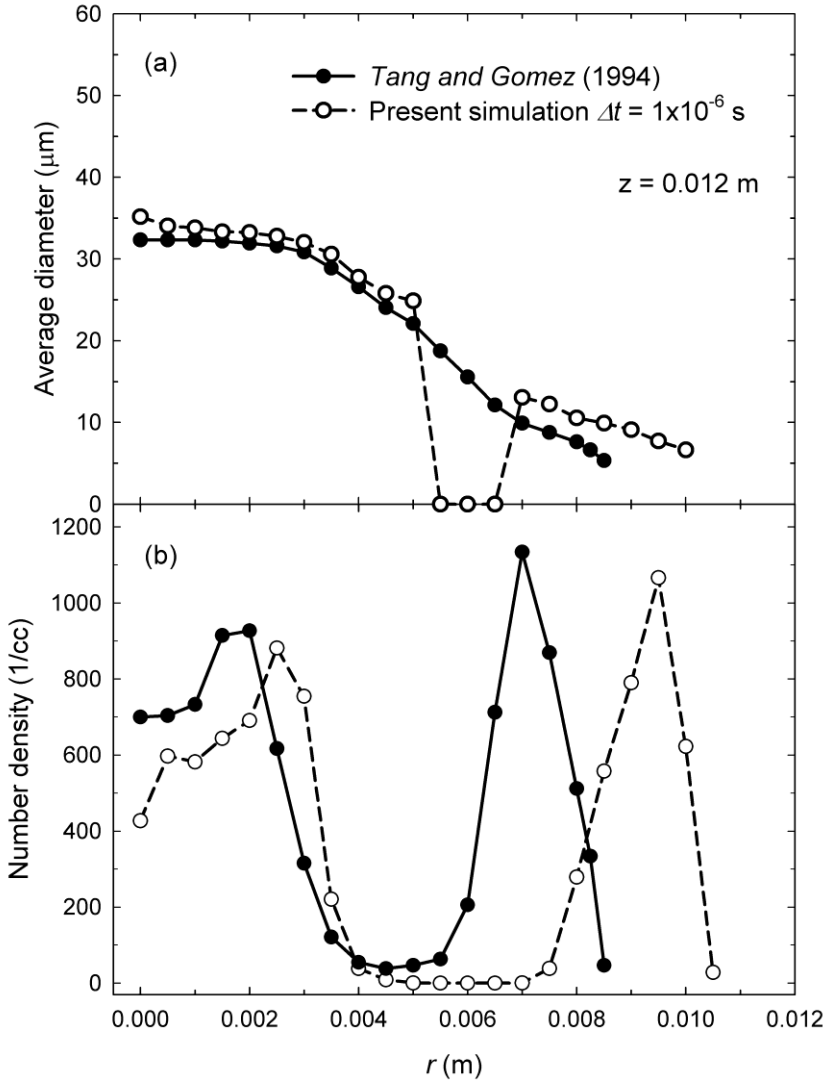

Fig. 9. Comparison of Case II complete simulation (using Base Code) versus experimental results: (a) Droplets average diameter; (b) Droplets number density versus radial coordinate and at z = 0.012 mm from the capillary tube exit.

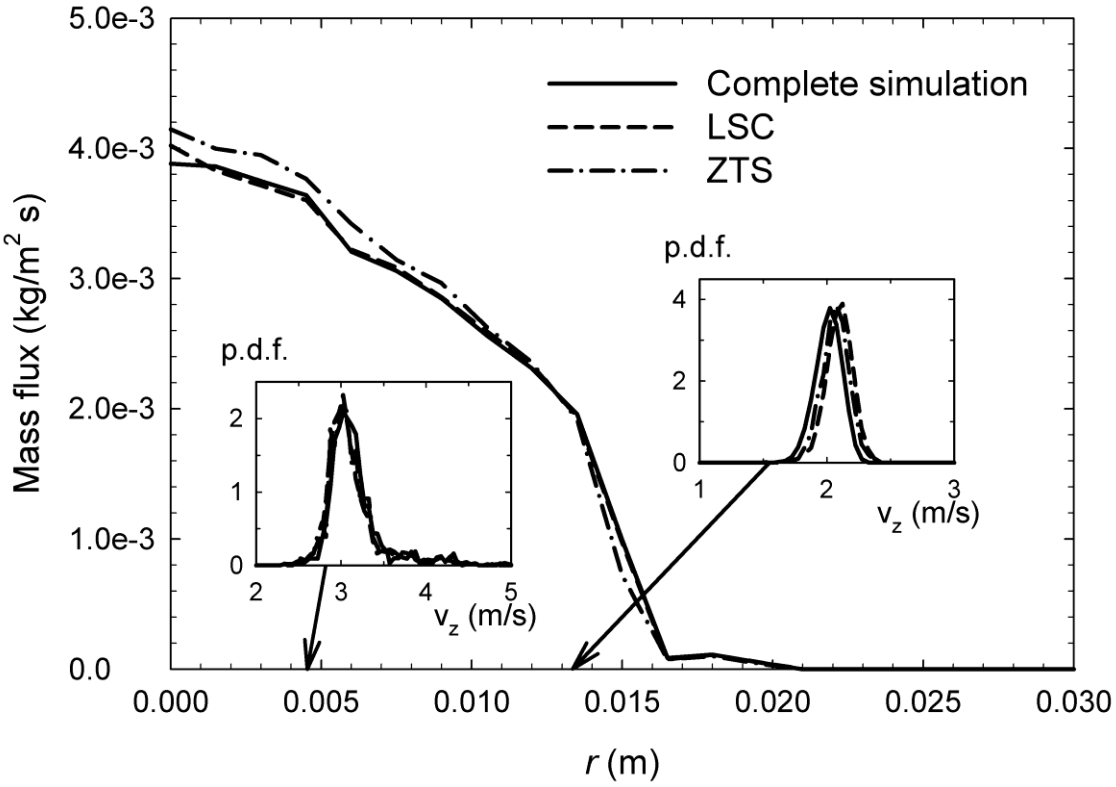

Fig. 10. Radial distribution of the mass flux due to droplets impinging on the collection plate, using different simulation methods for Case II. Insets show the p.d.f. (s/m) of axial droplet velocity located within $0.028 < z < 0.029$ m, and $0.004 < r < 0.005$ m (left) and $0.013 < r < 0.014$ m (right).